creative commons

COMMONS DEED

저작자표시-비영리-변경금지 2.0 대한민국

이용자는 아래의 조건을 따르는 경우에 한하여 자유롭게
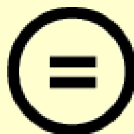
- 이 저작물을 복제, 배포, 전송, 전시, 공연 및 방송할 수 있습니다.

다음과 같은 조건을 따라야 합니다:

저작자표시. 귀하는 원저작자를 표시하여야 합니다.

비영리. 귀하는 이 저작물을 영리 목적으로 이용할 수 없습니다.

변경금지. 귀하는 이 저작물을 개작, 변형 또는 가공할 수 없습니다.

- 귀하는, 이 저작물의 재이용이나 배포의 경우, 이 저작물에 적용된 이용허락조건을 명확하게 나타내어야 합니다.
- 저작권자로부터 별도의 허가를 받으면 이러한 조건들은 적용되지 않습니다.

저작권법에 따른 이용자의 권리는 위의 내용에 의하여 영향을 받지 않습니다.

이것은 이용허락규약(Legal Code)을 이해하기 쉽게 요약한 것입니다.

Disclaimer

d Collection

Master's Thesis

Deformation of lyotropic chromonic

liquid crystal induced by cylindrical surface

Hyewon Kang

Department of Physics

Graduate School of UNIST

2020

Deformation of lyotropic chromonic
liquid crystal induced by cylindrical surface

Hyewon Kang

Department of Physics

Graduate School of UNIST

Deformation of lyotropic chromonic liquid crystal induced by cylindrical surface

A thesis

submitted to the Graduate School of UNIST

in partial fulfillment of the

requirements for the degree of

Master of Science

Hyewon Kang

12/14/2019

Approved by

_____

Advisor

Joonwoo Jeong

Deformation of lyotropic chromonic
liquid crystal induced by cylindrical surface

Hyewon Kang

This certifies that the thesis of Hyewon Kang is approved.

December 10, 2019

Signature

_____

Advisor: Joonwoo Jeong

Signature

_____

Hyuk Kyu Pak

Signature

_____

So Youn Kim

Abstract

Interfaces, where liquid crystals (LCs) is in contact with other materials, play a pivotal role in most LC-based applications such as displays and sensors. Physicochemical properties of interfaces impose a surface anchoring, and the geometry and topology of confining interfaces determine LC's director configuration and defects. To our interest, the concavely curved interface with anisotropic curvatures gives rise to a so-called surface-elasticity phenomenon.

   In this work, we report the director configuration around a cylindrical object embedded in nematic Sunset Yellow (SSY), a representative lyotropic chromonic LC with the large K24 modulus. The nematic SSY is sandwiched between two flat substrates, and a cylinder is placed in the SSY. The flat boundaries induce a homogeneous director field orthogonal to the cylinder's axis, whereas the cylinder aligns neighboring directors parallel to its axis, based on the theory related with K24. These boundary conditions result in the twist deformation near the cylinder, and we investigate the deformation experimentally and theoretically, and evaluate K24 of SSY.

Contents

Lists of figures

Lists of tables

Terms and abbreviations

LC	Liquid crystal
LCLC	Lyotropic chromonic liquid crystal
SSY	Sunset yellow

1   Introduction

1.1   Introduction

The liquid crystals (LCs) are defined as materials having LC phase between its crystal and liquid phases. For example, Fig.1 shows thermotropic LCs change their phase in the following order: crystal, LC, and
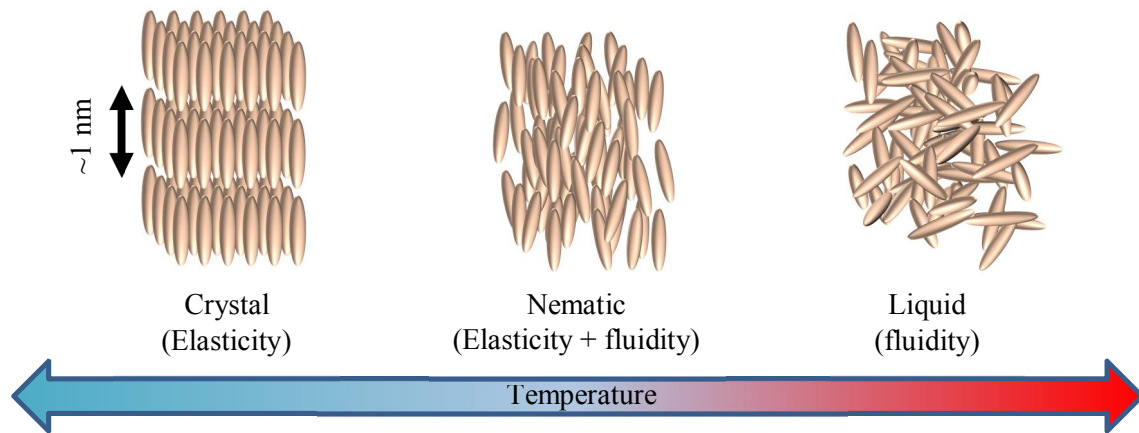
Figure 1. Phase diagram of thermotropic LCs

Thermotropic LCs (generally all LCs) show crystals' elasticity at a low temperature and fluidity at a high temperature. They show both features at an intermediate temperature range.

liquid phase as temperature increases. Not only the thermotropic LCs, but all other LC materials in LC phase, exhibit both elasticity of crystals and fluidity of liquids. Specifically, in one representative LC phase called nematic, molecules have only orientational order but positional order, and that orientational order is associated with the elasticity. The elasticity of nematic LCs is well pronounced in several experiments: (Nayani et al., 2015), (Ackerman, Van De Lagemaat, & Smalyukh, 2015). For example, the Nikkhou et.al, found a striking phenomenon of LC (Maryam Nikkhou et al., 2014), (Tasinkevych, Campbell, & Smalyukh, 2014), (M. Nikkhou, Škarabot, & Mušević, 2015): solitons and their interactions and theoretically explained how they originate from the orientational order of LC molecules around a cylindrical object. As in this research, analyzing orientational order of LC molecules enables us to understand various interesting LCs' phenomena. Therefore, it is regarded as fundamental process in many researches about static phenomena with LCs (Maryam Nikkhou et al., 2014), (M. Nikkhou, Gleeson, & Mušević, 2018), and is mostly performed by elastic free energy minimization developed by de Gennes. The elasticity of LCs can be described in terms of director, n, head-tail indistinguishable unit vector (Fig.2a). By definition, the director expresses the average orientation of local molecules, and the all orientations of local molecules in the whole space are simply dealt with by director field $n(x, y, z)$. Although being the most stable with homogeneous configuration (Fig.2b) in free space, director field stays deformed in response to interactions with confining walls, under the total free energy

minimization. The total free energy (F) consists of Oseen-Frank's elastic free energy and phenomenological free energy of anchoring on a surface.
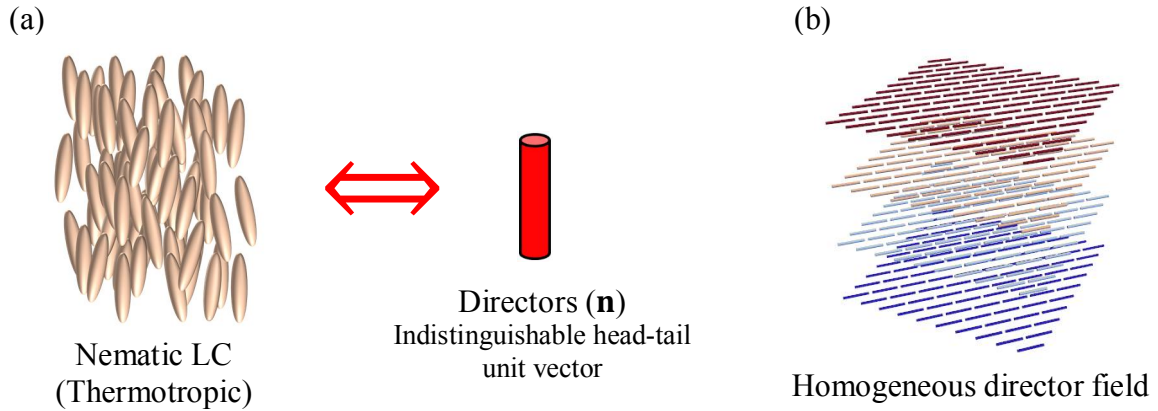
(a)   (b)

Directors (**n**)
Indistinguishable head-tail
unit vector

Nematic LC
(Thermotropic)

Homogeneous director field

Figure 2. Director representation of LC molecules' orientation.
(a) Director, defined as average orientations of local LC molecules can represent their orientational order. (b) The most stable state of LC molecules in free space is depicted by homogeneous director field.

$$F = \int_V dV \ [f_1 + f_2 + f_3] + \int_S dS \ [f_{24} + f_w] \qquad (1)$$

where f_1, f_2, f_3, and f_{24} denote elastic free energy densities for splay, twist, bend, and saddle-splay deformations of director field, respectively, and f_w denotes phenomenological anchoring free energy density on a boundary. Each free energy density is a function of director field and described explicitly in a background part. Although the total free energy comprises both surface and volume integral terms, many researches including (Maryam Nikkhou et al., 2014), (Čopar et al., 2016), (M. Nikkhou et al., 2018) left out the saddle-splay terms in minimization process. In those previous researches, the directors on the boundary were fixed so that the surface integral term became constant by assuming infinitely strong anchoring strength. However, that assumption should not be used when directors weakly anchor on a boundary, or when they can freely orient on a boundary, because the saddle-splay term may not be suppressed by weak anchoring strength. To tackle the directors' energetics with weak or little, void anchoring condition, saddle-splay term must undergo intense investigations. As a successful investigation (Jeong et al., 2015), our group proved the importance of saddle-splay term in the energetics of director field with degenerate anchoring condition, where boundary directors have no preferred orientation once they are tangential to the boundary. In that study, the resultant double-twist director configuration induced in cylinder that cannot occur regarding only bulk free energies was understood as a strong evidence for the considerable effect of saddle-splay term. Even though this study experimentally verified the effect of saddle-splay term for a concave cylindrical boundary, its result does not complete proving theoretical expression of saddle-splay term. Theoretically saddle-splay term

with planar anchoring condition on curved boundary, is written as

$$f_{24} = \frac{K_{24}}{2}(\kappa_1 n_1^2 + \kappa_2 n_2^2) \qquad (2)$$

where K_{24}, and κ_i ($i = 1\ or\ 2$) denote the elastic modulus of saddle-splay deformation and one of principal curvatures of boundary (Jeong et al., 2015). Due to the dependency on the principal curvatures, saddle-splay term is expected to change its effect when merely the sign of principal curvatures is changed, e.g, from concave to convex. This expectation was not verified by our group's previous experiment. To complement that previous study, we have been experimentally investigating if and how strongly the theoretical saddle-splay free energy works for convex, outer boundary of cylinder with degenerate anchoring condition, by observing and analyzing the director field configuration induced outside a thin cylinder. Unfortunately, it was challenging to identify and measure the saddle-splay free-energy's effect without advanced level of director field analysis. To brutally solve problems encountered, we limitedly evaluated the equilibrium director field at a simple level and found a way to answering our question. Based on our experiments and analysis, this thesis suggests theoretical saddle-splay term's effect for convex cylinder boundary is not easy to confirm. As a report of accomplishments during master's course, this thesis also covers our whole investigation and suggests some future works. Initially, we coincided our expectation with theoretical consequence of saddle-splay free energy. Saddle-splay term, Eqn. (2). is reduced to the following, with outer cylindrical boundary,

$$f_{24} = \frac{K_{24}}{2r}\sin^2(\Delta\phi_s) \qquad (3)$$

where r and $\Delta\phi_s$ denote radius of cylinder and the angle of a director in the boundary with the axis direction as depicted in Fig.3(a). For the simplicity, the directors only on the outer cylindrical boundary are referred to as surface directors, in this thesis. Apparently, when $\Delta\phi_s = 0$, f_{24} has the minimum value, resulting in the configuration where surface directors are parallel with cylinder's axis, referred
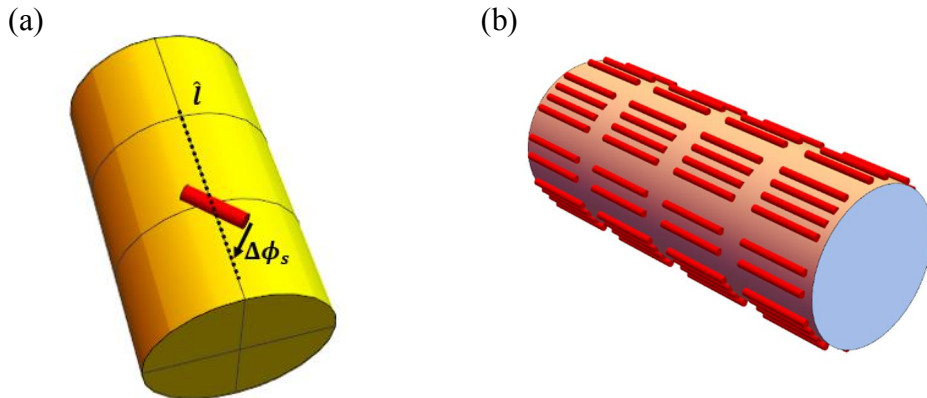

Figure 3. The effect and consequence of saddle-splay term minimization.
(a) Surface directors tend to align parallel with the cylinder's axis, to be the configuration of (b), when no other factors affect them.

13

to as uniaxial configuration, as depicted in Fig.3(b). And this saddle-splay term's energetical preference for the uniaxial configuration of surface directors is referred to as saddle-splay effect. If the eqn. (3) works, large enough K_{24} value might lead to the uniaxial configuration even with resists of the other elastic deformations. If the eqn. (3) works but K_{24} is not so critical, surface directors might have an oblique angle with the axis direction, when the other elastic deformations are against the saddle-splay effect. Fig.4(a) and (b) depict the expected configuration of surface directors with oblique angles, that is referred to as oblique configurations. Beside those pre-simulation of surface directors, this thesis also
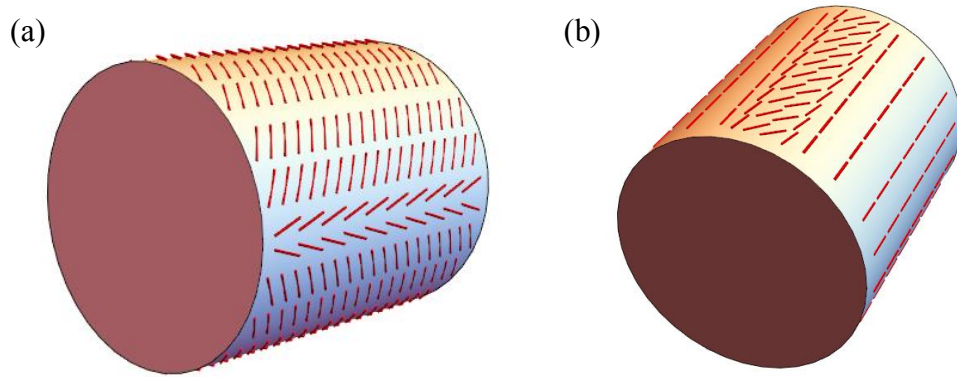
Figure 4. Two expected surface directors' configurations depending on K_{24}. Surface directors would have oblique angles when all the elastic deformations from the bulk compete with saddle-splay effect. Depending on K_{24}, the oblique angles surface directors would have will differ. Smaller K_{24} would result in (a) configuration rather than (b).

reports the whole research course of verifying and measuring saddle-splay effect, after a few explanatory parts for providing background concepts, and experimental details. Then, this thesis ends up with a suggestion to complete the ultimate research goal, future works, supplementary information, and appendix.

1.2 Background

1.2.1 Oseen-Frank free energy

Oseen-Frank free energy is a functional consisting of derivatives of director field, $\boldsymbol{n}$, expressed as eqn. (4) below. In bulk, deformations of director field can be written in terms of three principal deformations; splay, twist, and bend deformation, depicted as Fig. (5). Each deformation mode's associated elastic free energy account for bulk elastic free energy. On surface, saddle-splay deformation contributes to the surficial elastic free energy.

$$F = \int_V dV \ [f_1 + f_2 + f_3] + \int_S dS \ f_{24}$$

$$= \frac{1}{2} \int_V dV \ [K_1(\boldsymbol{n} \ \nabla \cdot \boldsymbol{n})^2 + K_2(\boldsymbol{n} \cdot \nabla \times \boldsymbol{n})^2 + K_3(\boldsymbol{n} \times \nabla \times \boldsymbol{n})^2]$$

$$-\frac{K_{24}}{2} \int_S d\boldsymbol{S} \cdot (\boldsymbol{n} \ \nabla \cdot \boldsymbol{n} + \boldsymbol{n} \times \nabla \times \boldsymbol{n}) \qquad (4)$$

where K_1, K_2, K_3, and K_{24} denote elastic moduli of splay, twist, bend, and saddle-splay deformations, respectively.

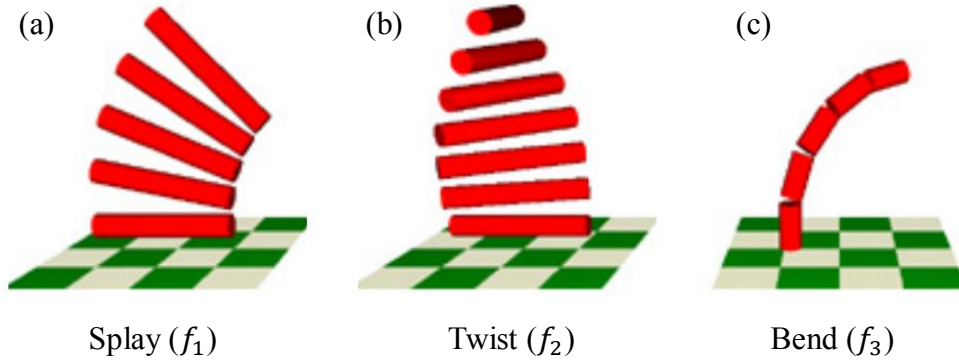(a) Splay (f_1) (b) Twist (f_2) (c) Bend (f_3)

Figure 5. Three principal deformations in bulk.
Any deformations of director field can be decomposed into splay (a), twist (b), and bend (c) deformations. Each mode contributes to the total free energy with its own associated free energy density that is in the form of harmonic potential of deformation multiplied by an elastic modulus.

1.2.2 Phenomenological anchoring free energy

In this thesis two kinds of anchoring conditions appear. Due to the physicochemical interaction between LC molecules and the boundary surface, molecules prefer orienting toward a specific direction on the surface. That preferred direction is referred to as easy axis. The average angular displacement of molecules from easy axis, i.e. director's angle with easy axis causes them unstable. Phenomenologically, their free energy is established in terms of director and easy axis.

$$\int_S dS \ f_w = -\frac{w}{2} \int_S dS(\boldsymbol{n} \cdot \hat{l})^2$$

where w and $\hat{l}$ denote anchoring coefficient and easy axis, respectively. In particular, when the easy axis is in plane of a surface, LC molecules are called to have planar anchoring condition on the surface, and their f_w is written as,

$$f_w = \frac{w}{2} \sin^2 \Delta\phi$$

where $\Delta\phi$ denotes the angle between easy axis and a director. Note that, f_w and f_{24} for

cylindrical surface with tangential condition, eqn. (3), are identical, implying saddle-splay effect can be interpreted as planar anchoring with its easy axis parallel with cylinder's axis, and with anchoring coefficient of K_{24}/r. In addition, when LC molecules prefer being tangential to a surface but without preference for azimuthal direction, the LC molecules are called to have degenerate planar anchoring on the surface, and their f_w is constant, because the easy axis in the case cannot be defined.
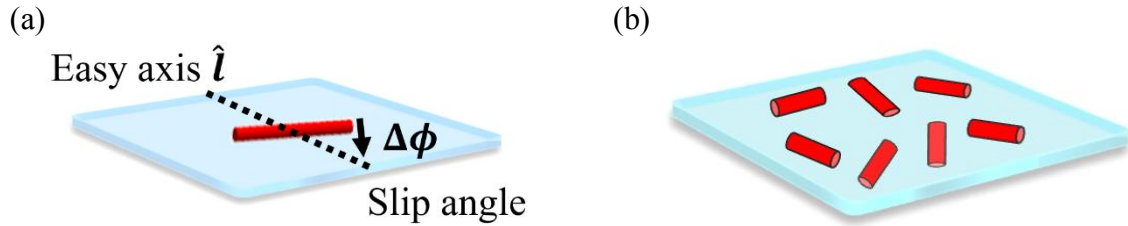
Figure 6. Two representative types of planar anchoring conditions.
(a) Planar anchoring. (b) Degenerate planar anchoring.

1.2.3 Defects

The equilibrium director field often has discontinuous structures inside, called defect. It forms as a result of free energy minimization. If director field can avoid its large deformation energy at the cost of free energy increase by defects or disclinations, director field forms defects. The defect can take various shape and one example is the loops shape called disclination. Normally, in the center of director field looks like Fig. 7(b), the disclination of winding number -1/2 forms. Another shape of defect is Boojum defects. When a spherical particle is in the homogeneous field of LC with degenerate planar anchoring, a pair of boojum defects, Fig.7 (a), form along the homogeneous field's direction.

Figure 7. Schematics of director field involving defects.
(a) Boojum defects (red) appear on the surface of spherical particle and along the homogeneous field. Conversely, visualize the 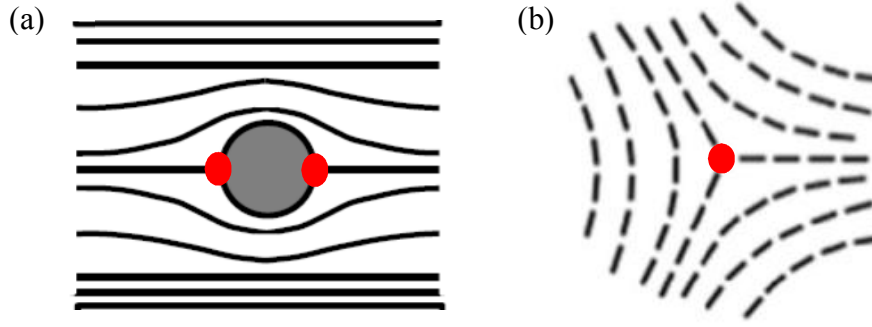direction of surrounding director field. (b) Conventionally, any director field that resembles (b) configuration, specified by the winding number of -1/2, has a disclination in its center (red).

1.2.4 Polarimetry for homogeneous field

When linearly polarized light propagates homogeneous director field, its polarization can transform depending on its initial polarization direction and thickness of director field. For example, in the simplest director field, homogenous field, the linearly polarized light does not change its polarization when it propagates with its polarization parallel or orthogonal to directors. However, when polarization of light at the entrance to homogeneous field (V_{in}) is neither parallel nor orthogonal to directors, the initial linear polarization decomposes into two orthogonal components and propagate at different speed owing to birefringence of LC (Δn). The phase retardance (Γ) of those decomposed lights develops during propagations, and, depending on the thickness (d) of homogeneous field, the final polarization at the exit of homogeneous field (V_{out}) could be elliptic. This polarization change is formulated by vectors and Jones matrix (Gwag, Lee, Han, Kim, & Yoon, 2002) as followings.

$$V_{out} = w_{homo} V_{in} \quad (5),$$

$$w_{homo} = R(-\phi_{in}) \begin{pmatrix} e^{-\frac{i\Gamma}{2}} & 0 \\ 0 & e^{\frac{i\Gamma}{2}} \end{pmatrix} R(\phi_{in}) ,$$

$$R(\phi_{in}) = \begin{pmatrix} cos\phi_{in} & sin\phi_{in} \\ -sin\phi_{in} & cos\phi_{in} \end{pmatrix} ,$$

$$\Gamma = 2\pi\Delta nd/\lambda$$

where λ and ϕ_{in} denote wavelength of light and the angle of initial polarization with

homogeneous field, respectively. Furthermore, the polarization of light can change depending on its incidence angle, experiencing more complex interaction with director fields other than homogeneous field.

1.2.5 Jones matrix calculation

The change of polarization of light can be calculated by Jones matrix when the director field light propagates through is known. The space can be regarded as a collection of infinitesimal cubic voxels. From that point of view, director field of known configuration occupying a space can be regarded as a collection of director field configurations occupying only each voxel. Since each voxel is infinitesimally small, the director field configuration in each voxel can be approximated as a homogeneous field orienting toward a known specific direction. Using Jones matrix representation for a homogeneous director field, one can obtain infinite number of vector relations for each voxel as eqn. (5). As depicted in Fig. 8. on the light path, a voxel passes polarized light to its neighbor. Therefore, the infinite number of vector relations for voxels on a single light path form a system of equations and join into the following vector relation.

$$V_{out} = w_n w_{n-1} \cdots w_2 w_1 V_{in} \quad , (n \to \infty)$$

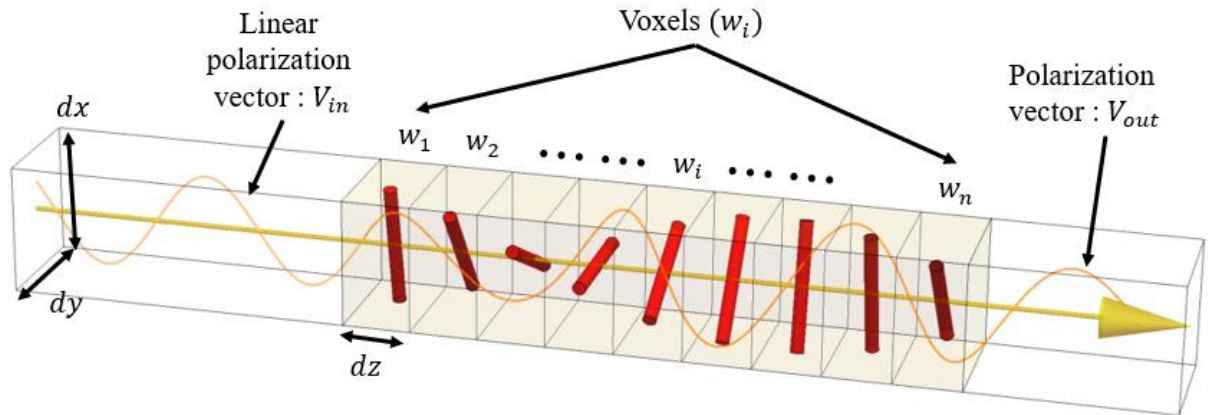As long as the director field and, hence, w_i are known, V_{out} can be calculated.

Figure 8. Idea of Jones matrix calculation for a known director field.

Any known director field can be regarded as a series of infinitesimally small homogeneous field toward a known direction. Using Jones vector and matrix, the input and output polarization vector can be related.

1.2.6 Lyotropic chromonic liquid crystals

Lyotropic chromonic liquid crystals (LCLCs) generally have discotic molecules. One representative LCLC is Sunset yellow (SSY) depicted in Fig. 9(a). While thermotropic LCs' phase is only governed by temperature as Fig. 1, LCLCs' phase depends on both temperature and their concentration in medium and that two dependencies are referred to as the term lyotropic. Fig. 9(b). shows SSY's phase diagram (Davidson et al., 2017), and it shows the temperature and concentration in water ranges for each phase: isotropic, nematic, and columnar. As another difference from thermotropic LCs, in nematic and columnar phases, SSY (generally, LCLC) molecules form elongated structures, called aggregates, due to non-covalent attractions between faces of SSY (LCLC) molecular discs. This formation of aggregates is referred to as the term chromonic. Although LCLCs molecular structure and thus, molecular movement and orientation are somewhat different from that of thermotropic LCs, aggregates of LCLCs show similar behavior with molecules of thermotropic LC. Likewise, director can be also defined as the average orientation of aggregates in a local space.
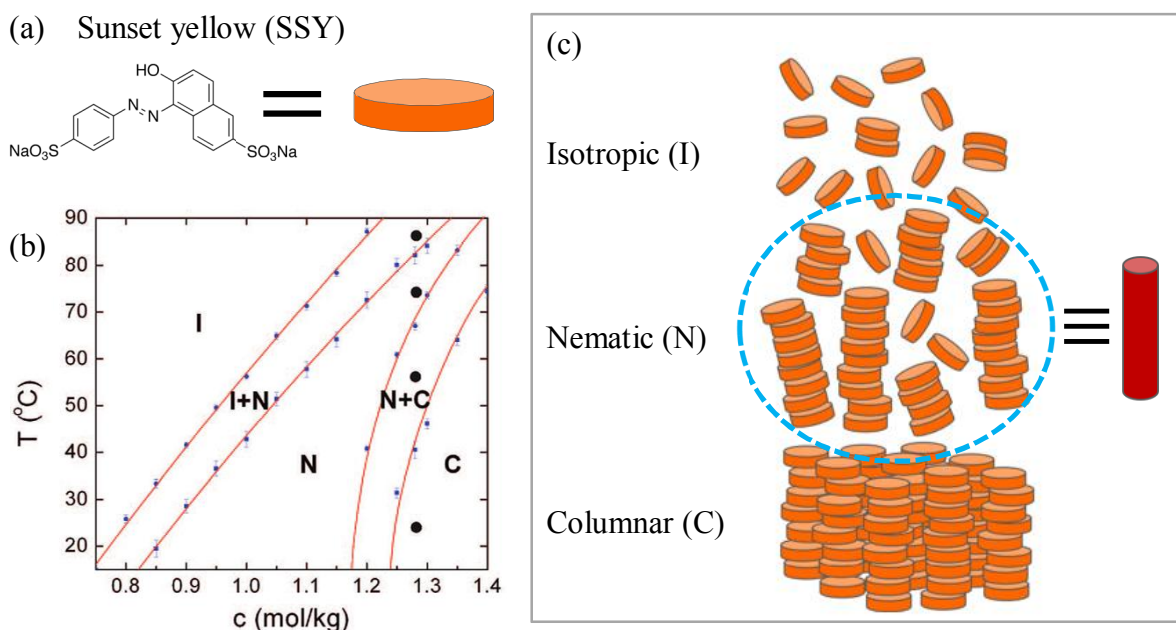

Figure 9. Sunset yellow in the class of lyotropic chromonic liquid crystal.

2   Experimental setup, method & materials

2.1   Ingredients for cells

The cell composing ingredients: glass fibers, spacers, and slide glasses, needed some treatments or cleaning before uses. a glass fiber of $13\mu m$ diameters, purchased from Fiber man, was sonicated with ethanol and IPA, successively. We used the sonicator 3800, from Branson, and all sonication was performed with maximum power longer than three minutes. The sonicated fiber further undergoes plasma cleaning. Using plasma cleaning aperture, CUTE from Femtoscience, the fiber was exposed to the air plasma generated with following aperture settings: 100kHz generating frequency, 100W generating power, longer than two minutes operation time, about 0.13 torr chamber pressure. Second, spacers are selected for having chemical stability and uniform thickness. We chose Kapton's polyimide films of thickness 25 and $50\mu m$, and optical fibers of total thickness 89, 124, and $152\mu m$ from Molex. When these spacers were going to contact with LCs, they underwent ethanol and IPA sonication. Finally, a pair of slide glasses, from Duran, were polished with Trizact foam abrasive disc (P3000), from 3M, either lengthwise or crosswise, more than 30 times of movement. While polishing, about 2kPa pressure on average was transferred onto the slide glass. We presume that more than 30times of movements that could not perfectly coincide each time make satisfactory uniform fine scratches on slide glasses. With those three ingredients prepared, we made four types of cells, named as parallel cell, orthogonal cell, suspended cell, and polymer-wet cell.

2.2   Sample preparation

SSY, from Sigma-Aldrich, having some impurities needs purification. The purification is conventional for SSY using experiments, so we followed the purification process done in other preceding researches (Horowitz, Janowitz, Modic, Heiney, & Collings, 2005). Then, the purified SSY powders are dissolved in deionized water to the 30.0wt% at which SSY solution is in nematic phase in room temperature, $23^{o}C$. This SSY solution is kept in isotropic phase until being injected into the cell.

2.3   Cell production
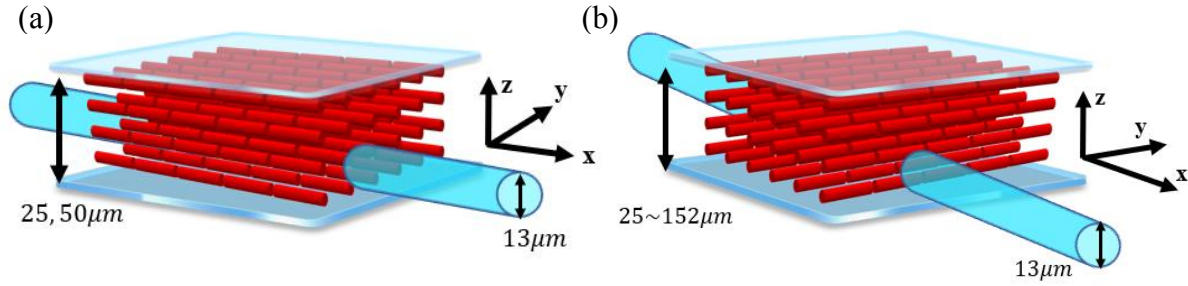

(a)

(b)

25, 50μm

13μm

25~152μm

13μm

Figure 10. Final structure of parallel cell (a) and orthogonal cell (b).

With the cell ingredients, parallel cell, orthogonal cell, suspended cell, and polymer-wet cell are assembled, and then, after several steps, become ready for experiments. For parallel (orthogonal) cell assembly, a glass fiber was laid in the middle of lengthwise (crosswise) polished slide glass with its axis parallel (orthogonal) with polishing direction. Then the both ends of the fiber were bound onto the bottom slide glass, ensuring the fiber straightened, using scotch tape. Spacers, wet by Epoxy, from Loctite, were put along the longer edges of the slide glass. Another polished slide glass was put only on the wet spacers, with its polished direction parallel with the bottom one. Before complete curing of epoxy, the cell was strongly compressed by clips. The assembly of suspended cells is slightly different from that of orthogonal cells. Instead of bounding the both ends of the fibers to the bottom, it was held off the bottom using smaller supporting spacers, again ensuring the fiber straightened and orthogonal to the polishing direction. The polymer-wet cell is assembled simply by wetting the fiber of orthogonal cell with Noa89 liquid polymer, from Norland. Being different from other cells, polymer-wet cell is completed by the injection of SSY solution. Due to Rayleigh instability, polymer wetting breaks up into numerous droplets once SSY is injected. Accidently, a few droplets could stay on the top of the fiber. Since those droplets are the key in some experiments, the polymer-wet cell production should be repeated until a few droplets are yielded in the end. As polymer-wet cell is done, the assemblies of the other cells are followed by SSY-solution injection. As soon as SSY completely fills a cell's space, the cell must be sealed immediately with Epoxy to prevent concentration change due to the evaporation of water. After the epoxy cured, all cells were heated up to isotropic phase in the oven, and then quenched in the room temperature. The observation was awaited by 4~5 hours for the relaxation of director field.

2.4   Coordinate designation for cells

In every experiment and analysis, directions and angles are described in x, y, z-coordinate where x-axis is parallel with fiber's axis, x, y-plane is the bottom polished surface, and the positive z-axis is toward the top.

2.5   Optical microscopy

Upright microscope, from Olympus, was used for imagining with objective lens, from Olympus, whose magnification of 10x, 20x, or 60x. For polarized optical microscopy images (POM images) that are images taken with both polarizer and analyzer, the LED light from the source is linearly polarized at the polarizer, then becomes collimated at the condenser. After the light passes the LC cell, it encounters analyzer, and only surviving components reaches the panels of CCD. For bright field images, polarizer and analyzer were off.

2.6   Polarimetry setup

In the polarimetry of microscope, light path is set to be the positive z-direction, and the rotations of polarizer, analyzer and the sample plate are restricted in x-y plane. The orientational angles of the polarizer and analyzer are measured in positive sign counter-clockwise from x-axis. Especially, for successive polarimetry imaging, the polarizer is rotated from the angle 0° to 180°, with 10° step increasement, while analyzer was fixed at 90°.

3   Result & Discussion

3.1   Director field and surface directors

In the parallel cell, the equilibrium director field and surface directors are homogeneous to x-direction and uniaxial, respectively. The POM image of a parallel cell, Fig. 11, has uniform and completely dark brightness throughout the field of view. Based on the polarimetry analysis, this result must be produced from the homogeneous director field in x-direction. If the equilibrium surface directors are not uniaxial, the director field in the bulk must have deformation around the fiber with respect to minimization of the total free energy. In consequence, that will necessarily make POM image have irregular brightness other than uniform, completely dark brightness. Therefore, it is sure the surface directors reach uniaxial configuration. Yet, the cause of the uniaxial alignment is in question.

The uniaxial surface directors do not assure the existence of saddle-splay effect. The uniaxial surface
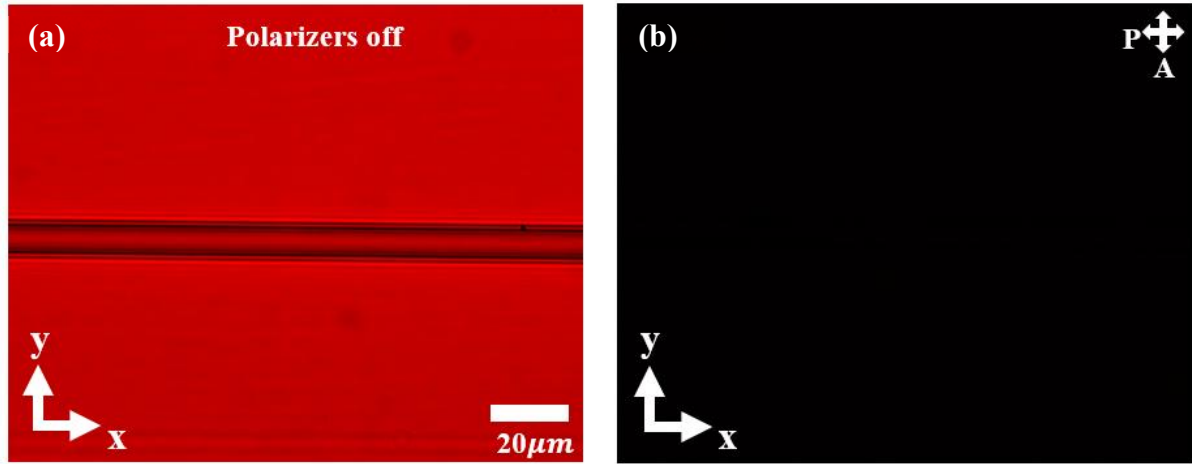

Figure 11. Bright field image (a) and POM image (b) of parallel cell.
P and A denote direction of polarizer and analyzer.

directors proved by the POM image is the very director configuration saddle-splay effect alone leads to. Also, if surface directors were subject to any unidentified orientational forces toward any non-axial direction, uniaxial configuration must not appear. Yet, unfortunately, void saddle-splay effect, i.e. $K_{24} = 0$, can be the case, because, without saddle-splay effect, free energy minimization along with degenerate planar anchoring let the surrounding homogeneous field forces the surface directors to be uniaxial. For either zero or positive K_{24} value, surface directors have uniaxial configuration, so conversely uniaxial surface directors do not prove saddle-splay effect exists. To determine K_{24} value, orthogonal cell experiment was conducted, and a complex director field emerged as a result. For simplicity, we refer to the surface directors on the top (side) of the fiber as top (side) surface directors.

23

3.2 Twist deformation in orthogonal cells

In the orthogonal cell, top surface directors have an oblique angle with the x-direction. Assuming the polymer-wet cell induces the almost identical director field with that of the orthogonal cell, the POMs of polymer-wet cell were obtained as Fig. 12. In these POMs, Boojum defects direct local director field. Therefore, top surface directors are confirmed to have an oblique orientation. This orientation of top surface directors helps figuring out the surrounding director field.
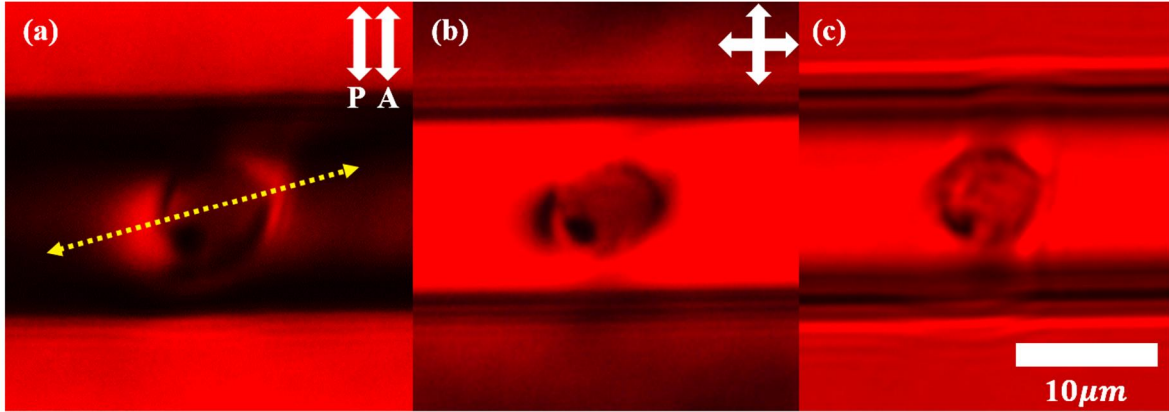

Figure 12. POMs of Boojum defects.

(a), (b), and (c) with different polarimetry setup, the same boojum defects were observed. They indicate the orientation of top surface directors.

In an orthogonal cell, the director field is characterized by twist deformation over a domain near the fiber. POM image of an orthogonal cell, Fig. 13(a). shows the speckle pattern of director field that resembles haystack of various brightness. In that a speckle pattern in a region roughly exhibit the local director field (Jeong et al., 2015), we can see, along the fiber, the biased director field in the domain of a certain y-directional width where the fiber lies in the center. Slightly over the fiber, that biased field is in accordance with the oblique top surface directors, while obeying free energy minimization. In a y-directionally remote region, the oblique bias of directors fades away to the y-direction as depicted in Fig. 13(b). However, that decay of oblique orientation, interpreted as decreased influence of the fiber, does not belongs to y-direction only, but to z-direction. Thus, it is evident that the decay of the oblique orientation develops twist deformation into the z-direction, and it locates on the domain of biased director field.
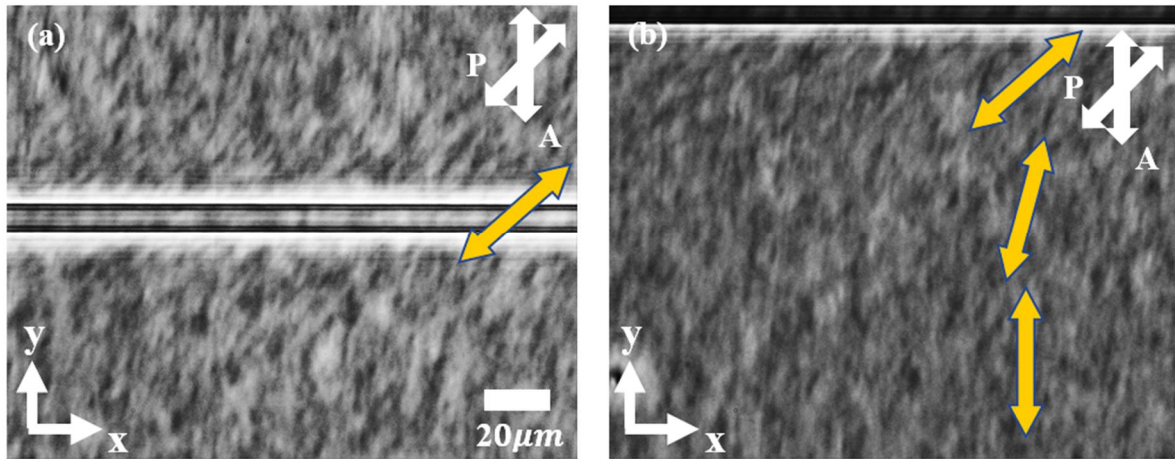
Figure 13. Speckle patterns formed near the fiber.

Speckle patterns also indicate director field by its texture.

The twist nature of the director field is supported by the symmetry breaking phenomenon. The degree of freedom provides the domain with the equal chance to have twist deformation of either the left or right handedness. Accordingly, the two different handed twist domains appeared almost equally, and an interesting defect settles between the neighboring domains of different handedness as in Fig.14. Those defects also appear with several properties similar with the result reported in (Čopar et al., 2016). Now that we have understood the conformation the director field has in an orthogonal cell, the rest of this thesis cope with questions about its origin and the role of saddle-splay effect.
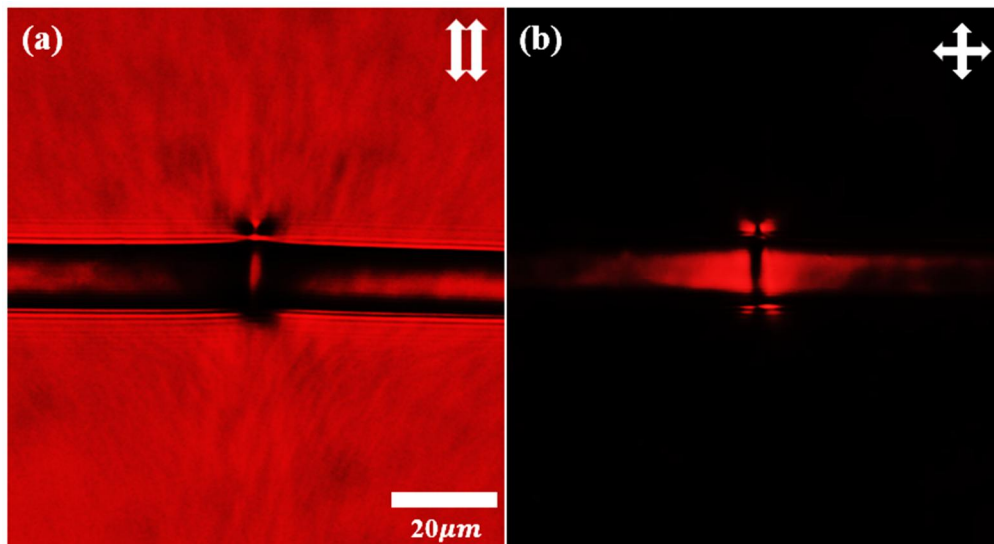

Figure 14. A defect between twist domains of different handedness.

The saddle-splay effect is not yet able to identify, owing to unquantified bulk free deformation energy. The problem in identifying saddle-splay effect in parallel cells extends to the study on director field in orthogonal cells. Without the saddle-splay term, degenerate planar anchoring and bulk free energy minimization force side surface directors (side of the cylinder) to have considerable x-component, i.e. escape in x-direction, to prevent formation of disclination with -1/2 winding number. Obeying only the bulk free energy minimization, this x-directionally escaped side surface directors can cause top surface directors to have unignorable x-component that is accompanied by biased boojum defects as Fig. 12. If the saddle-splay effect is additionally considered, only the quantity of the oblique orientation directors in the bulk and surfaces have will be changed. Again, regardless of existence of saddle-splay effect, surface directors have oblique orientation. On this account, to examine the contribution of saddle-splay effect to the surface directors, first, we studied the twist deformation and the orientation of top surface directors by following the preceding research (Mcginn et al., 2013).

3.3   Quantitative analysis of director field

The twist deformation above the fiber has a non-linear profile. We performed successive polarimetry experiment and fit the intensity change with an ansatz function derived from linear twist model as in the preceding research (Mcginn et al., 2013). The fitting parameters are listed in Table. 1 for each cell gap. The both parameters ϕ_{bot} and ϕ_{top}, denoting the angle of top surface directors with the x-direction and that of directors on the top flat boundary (glass substrate) with its easy axis, respectively, are apparently irrelevant with cell gap increasement. However, according to the previous report, both ϕ_{bot} and ϕ_{top} must decrease with the cell gap increasing. Because those fitting parameters do not behave as the previous study proved, we believe the twist profile is non-linear. To obtain exact function of non-linear twist, we theoretically studied the director field but in a simple manner.

Table 1. The fitting parameters

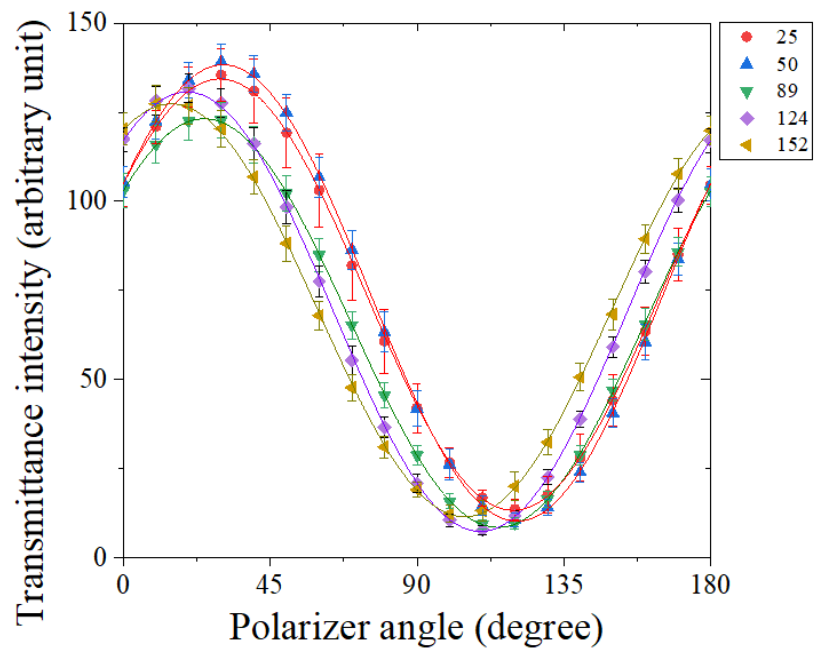| Measurement error ($\pm 2.5^{o}$)	$25\mu m$	$50\mu m$	$89\mu m$	$124\mu m$	$152\mu m$
ϕ_{top} (degree)	77	76	74	77	74
ϕ_{bot} (degree)	36	32	17	18	12

Figure 15. Intensity change date and fitting with transmittance from linear twist model.

In attempt to find approximate director field, we reduced the free energy minimization to Laplace equation of directors' orientation angle, using several assumptions and simplification. The reducing process was initiated with several intuitions and facts. As we discussed above, directors around the fiber have a sizable x-component due to the escape, so the large x-component reduces upper bounds of y and z components. As for another intuition, real director field seen from the x-direction must resemble streamline of a fluid that pass over a speed bump as depicted in Fig. 16. The height of a directors' streamline must have a proportional relation with the radius of the fiber. The radius to cell gap ratios
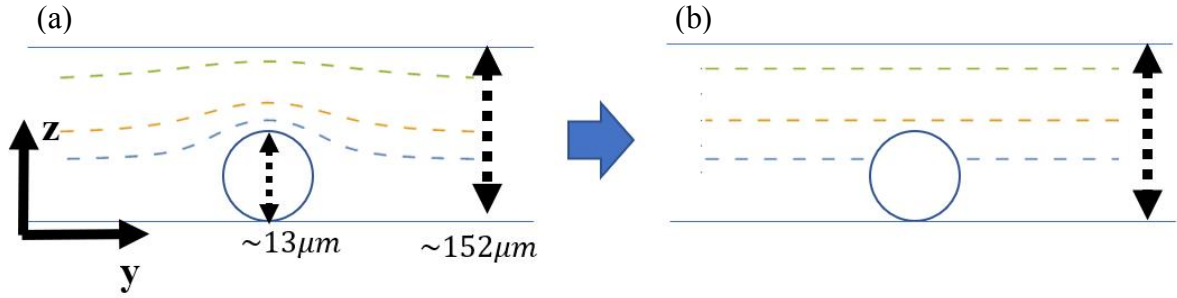

Figure 16. The schematics for the simplification of $n_z = 0$.

ranging from 0.04 to 0.24 suggests the height of a streamline as well as n_z along a streamline of directors could be insignificant, especially in large cell gap. Based on those two intuitions, we anticipated small z-component of directors near the fiber and neglected every director's z-component ($n_z = 0$). Under that rather naive simplification directors can have only azimuthal angle, ϕ, around z-direction. Then the director can be written in terms of the angle of directors, ϕ, as $\boldsymbol{n} = (cos\phi, sin\phi, 0)$. Further, based on the value of K_1 and K_3 of SSY (Zhou et al., 2012) and the symmetry in the orthogonal cell, we assumed the identical splay and bend moduli, i.e. $K = K_1 = K_3$ and $\partial_x \boldsymbol{n} = 0$, respectively. These, one simplification and two assumptions reduce the Euler-Lagrange equation of the bulk free energy functional into the 2-dimensional Laplace equation of $\phi(y, \sqrt{K/K_2}z)$ with scaled z variable. We solved the Laplace equation analytically and numerically with additional simplifications.

28

Analytic solution obtained with additional simplifications of boundary conditions shows non-linear twist deformation. To analytically solve the Laplace equation, we further simplified the geometry of this equation such that the half cylinder is on the bottom in place of the whole cylinder and the cell gap expands to infinity. Finally, we assumed the simplest boundary conditions: for the directors on the bottom flat boundary, $\phi = 90^o$, and for the surface directors, $\phi = 0^o$ (uniaxial), each of which corresponds to infinite w and K_{24}, respectively. The solution and twist profile above the fiber $\phi(0, z_s)$, were obtained as eqn. (6) below, and Fig. 18., where z_s denotes distance in the z-direction from the top of the cylindrical boundary. Beyond this simplified model, we attempted to apply finite w and K_{24} instead of their infinity limit, so that directors on the boundaries can have an angle neither 0 nor 90°.
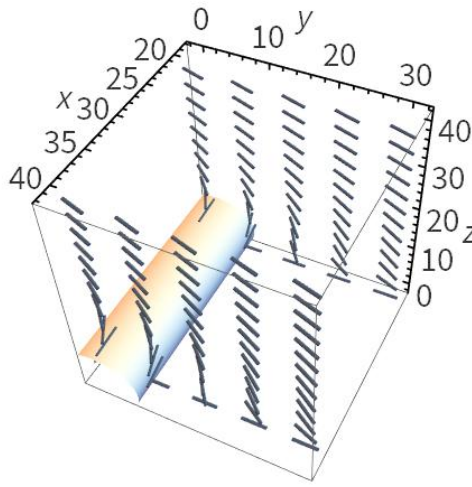

Figure 17. Director field plot from analytic solution.

$$\phi(x,s) = tan^{-1}\left(\frac{sin2s}{sinh2x}\right) \quad, \qquad x + i\,s = \frac{1}{2}cosh^{-1}\left(0.5\left(\frac{y'}{y'^2+z'^2} + y'\right) + 0.5\,i(z' - \frac{z'}{y'^2+z'^2})\right) \qquad (6)$$

where y' and z' are again a function of y and z. The explicit relations between variables as well as the full y, z representation of the solution is provided in appendix.

Saddle-splay effect cannot be adopted without a limit into the boundary condition of the Laplace equation owing to the conflict with an early-made requirement for the directors. Assuming that saddle-splay effect exists, the release of K_{24} from infinity leads to a certain oblique configuration of surface directors. If side surface directors have oblique orientation similar with Fig. 4(a), they inevitably violate the early applied simplification of $n_z = 0$, while having considerable z-component. Preserving that simplification to keep the Laplace equation in 2-dimension, we investigated only a limited possibility in which surface directors can have oblique angle only in approximately flat region of the fiber, referred to as band, but uniaxially in the other region of the fiber's surface, as depicted in Fig. 19. With this new heterogeneous boundary condition, we continued solving the Laplace equation, however, numerically because of the analytically challenging boundary conditions.
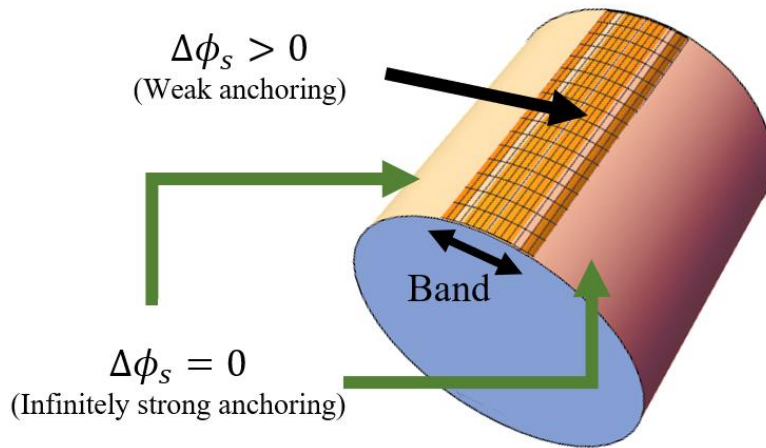

Figure 18. Heterogeneous boundary for numerical approach.

In contrast with the analytical approach, numerical approach with the new heterogeneous boundary condition adopted the real geometry of the boundary without any simplification. Because of the advantage of numerical analysis, the boundary for the Laplace equation mimics the real system geometry. It includes a finite cell gap (d) and the whole cylinder on the bottom substrate. To the top and bottom flat boundaries, we imposed the boundary condition,

$$K_2 \left.\frac{\partial \phi}{\partial z}\right|_{z=0,d} = \pm \frac{w}{2} sin2(\phi - \pi/2)|_{z=0,d} \quad , \qquad \begin{cases} z = 0: \ + \\ z = d: \ - \end{cases}$$

which is the consequence of minimization of anchoring free energy. The surface directors in the band of the heterogeneous boundary is under the boundary condition of the similar form,

$$K_2 \frac{\partial \phi}{\partial z}\Big|_{z\sim 2r} = \frac{K_{24}}{2r} sin2\phi|_{z\sim 2r}$$

which is the consequence of minimization of saddle-splay free energy. As described above, the other region of the heterogeneous boundary has the condition of $\phi = 0$. Using finite element method function encoded in Mathematica 12, we found the numerical solution and, thus, director field (Fig. 20). Next, we studied twist profile changes depending on parameters.
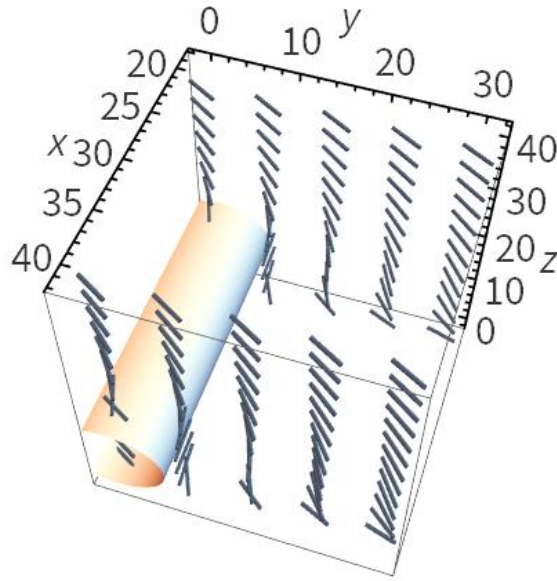

Figure 19. Director field plot from numerical solution

Nonlinear twist profiles above the fiber change to different extent depending on each parameter. The numerical solutions are obtained for each parameter set including cell gap, orientation of easy axes of flat boundaries, anchoring coefficient, saddle-splay modulus, birefringence, and the bandwidth. The most impactful parameter on the twist profile is cell gap. As the cell gap increases with the other parameters fixed, the middle part of the twist profile curves as shown in Fig. 20. For comparison, the
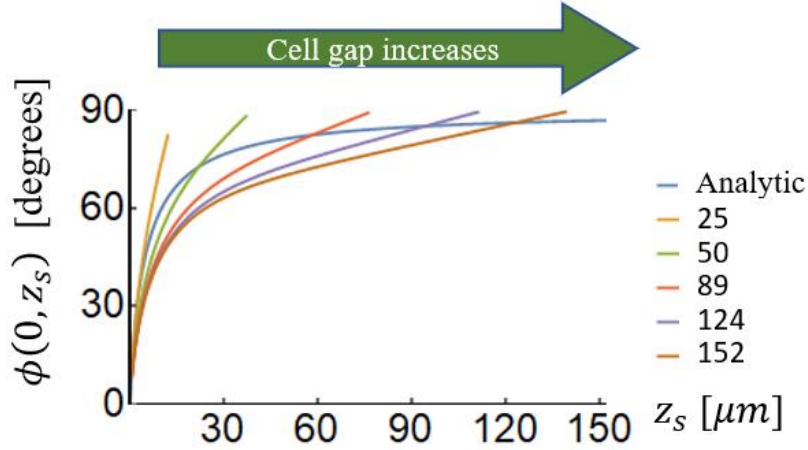

Figure 20. Cell gap dependency of twist profile.

profile of analytic solution is plotted together. The rest of the parameters were not as influential on the twist profile as the cell gap as shown in in Fig. 22. and Fig. 21. Among every parameter set, one parameter set that best fit the intensity change is going to be determined using Jones matrix in future.
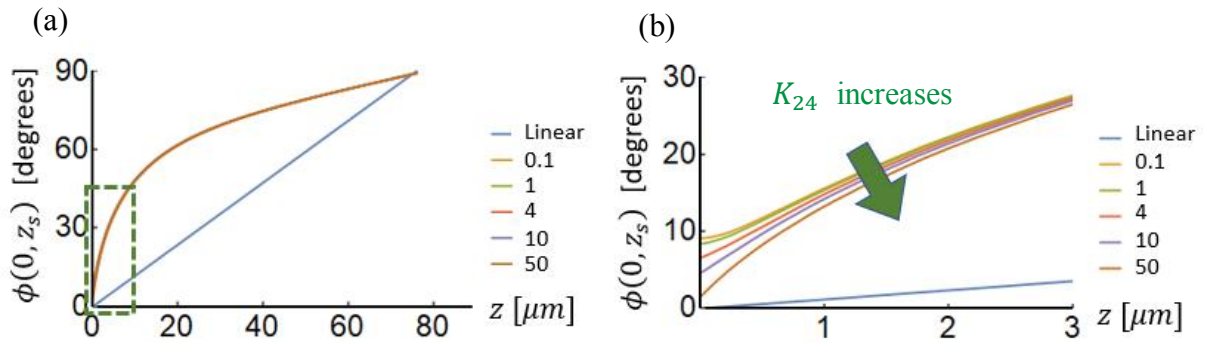

Figure 21. K_{24} dependency of twist profile.
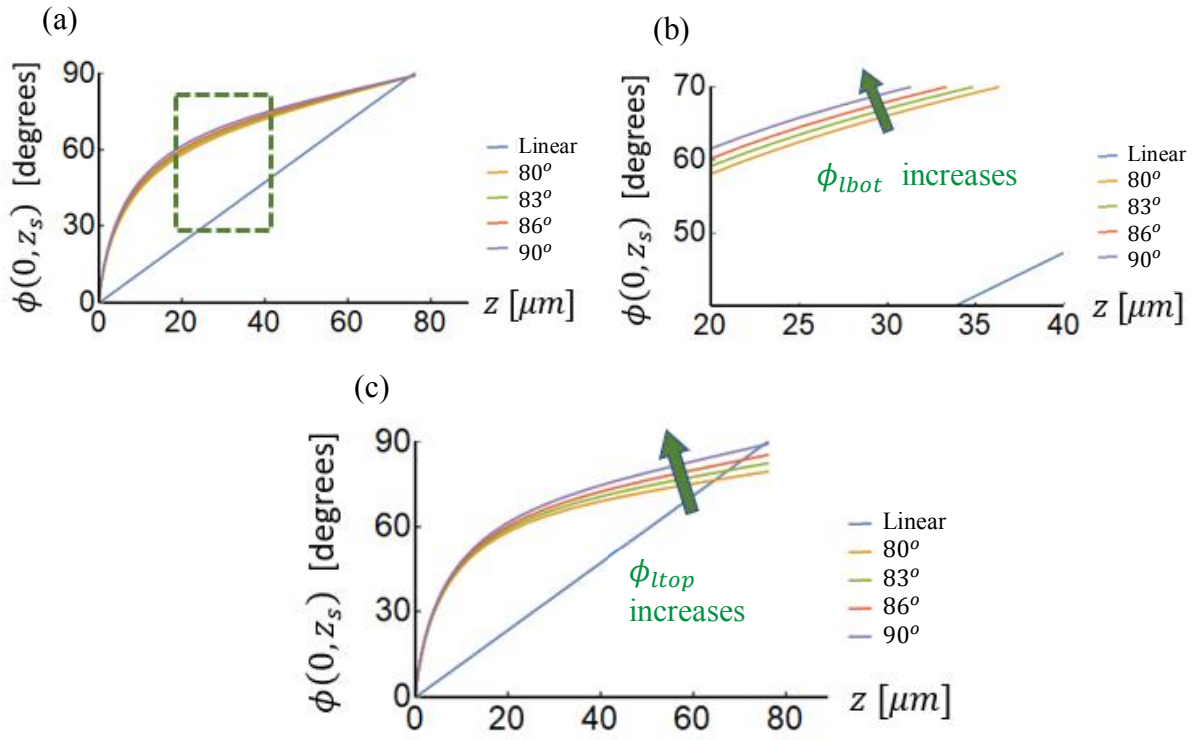(a) The part in green box is enlarged in (b). K_{24} does not affect the profile significantly.

Figure 22. Easy axes dependency of twist profile.

ϕ_{ltop} and ϕ_{lbot} denote the orientation of easy axis on the top and bottom substrates, respectively.
(a) The part in green box is enlarged in (b).

Background intensity fitting prior to the fitting at fiber's center can help parameter selection. Jones matrix intensity fitting with the numerical twist profile gives us a set of parameters with an error from the intensity change data. Even if numerical solution cannot demonstrate fine structures of real director field, its under-achieving performance can be compensated by fitting intensity change over wider region. For example, as in Fig. 23, in the many regions remote from the fiber, i.e. background, z-directional directors' angle profile is of little twist, and it is sure to be little dependent on K_{24} and bandwidth because of the remote distance from the fiber. Thus, the rest of dependent parameters may be easily determined by performing the fitting for many regions at background. Having narrowed selection of parameter set, the fitting for the region in the fiber's center can work with reliable parameters pre-determined.
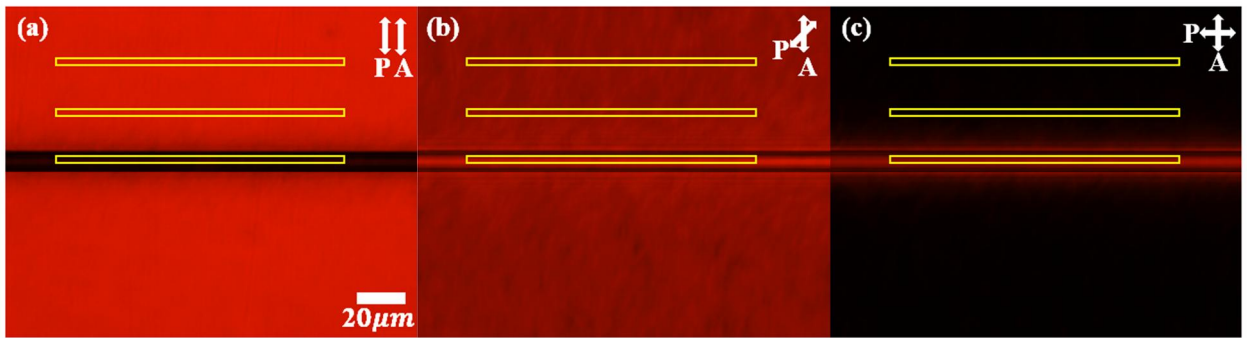

Figure 23. POMs with different intensity depending on polarizer's angle.

The intensity change was measured only in the yellow box above the fiber.
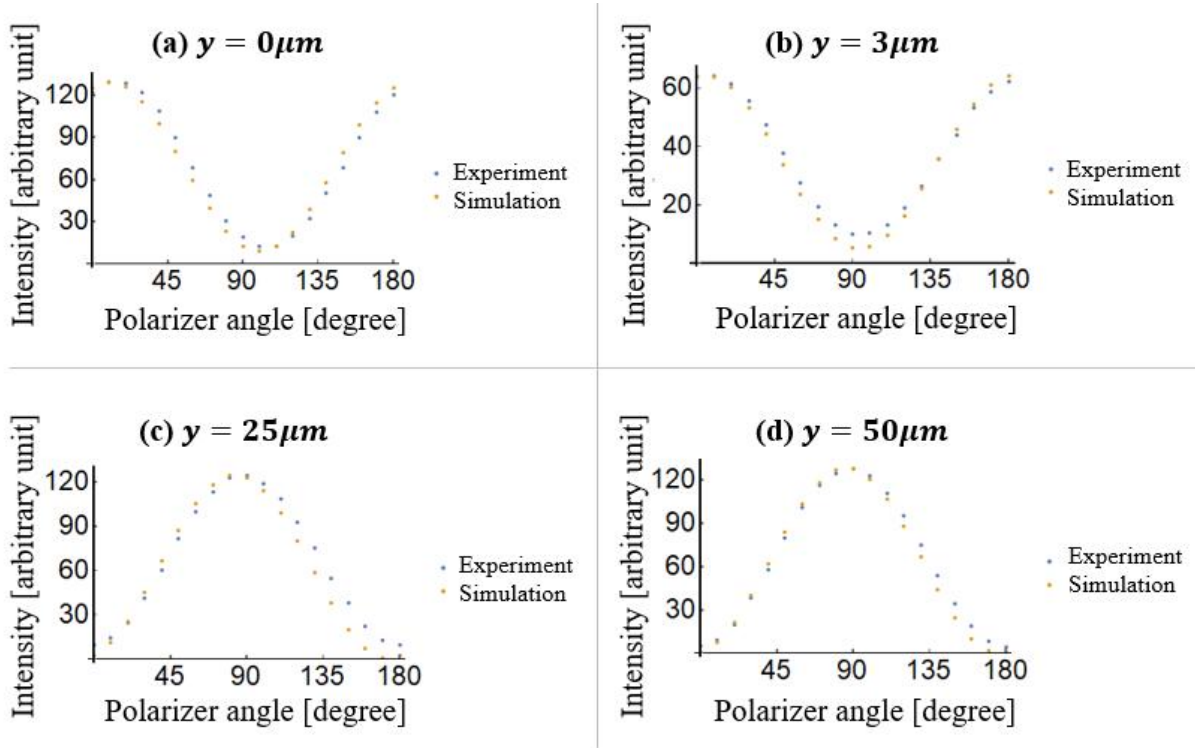

Figure 24. Intensity change fitting being done with numerical model.

The numerical analysis and intensity fitting may enable us to roughly evaluate saddle-splay effect. With several simplifications and assumptions, we numerically demonstrated rough director field configuration and calculated transmittance of linearly polarized light. Although not accomplished yet, comparing the calculation with the intensity change data, i.e. fitting, will be completed following the strategy above, and provide us with K_{24}. If the resultant K_{24} value is about zero, it could be concluded saddle-splay effect does not exist outside of the fiber, or simplifications were not appropriate. Otherwise, our estimation might be one reference of K_{24} value.

4 Conclusion

Although we confirmed the equilibrium director field in both parallel cell and orthogonal cell, we could not qualitatively identify saddle-splay effect because of the interplay between bulk elastic deformations. To quantify the saddle-splay effect and the other effects on surface directors, we demonstrated a theoretical approach, but it has not been completed and needs further developments. In addition to the necessity for researches on saddle-splay in pursuit of better description of director field with degenerate planar anchoring or weak anchoring condition, unclear origin of saddle-splay effect can be also attraction for many enterprising physicists. Similar to saddle-splay term's origin, the detail mechanism in which the surface grooves induce weak, planar anchoring of some LCs, is also a mystery yet. Asking any answers, we carefully suggest a question: saddle-splay effect and weak, planar anchoring by grooves that have the same keywords of surface and curvature, may be interconnected with a governing principle.

5 Future work

The experiment and theoretical analysis can be improved in several ways. The experiment can be implemented with the fibers of various radius whose surface is confirmed to have degenerate planar anchoring condition, or with half-cylinder glass rod of various radius, produced by Hilgenberg, that requires the confirmation of the degenerate condition. By those changes of the boundary, the radius dependency of saddle-splay effect can be also verified. Also, the objective lens needs higher magnification especially for imaging with higher precision and imaging thinner fibers than the fibers in the current experiments. In theoretical approach, if possible, the minimizing the total free energy functional leading to the differential equations of director field will be formulated in three-dimension with reliable assumptions. Analytically or numerically, director field will be calculated with and without saddle-splay term separately to contrast each result, with the other.

6 Supplementary information

By thorough plasma-cleaning, glass fiber's surface chemical layer must be removed to achieve degenerate anchoring condition. Most glass fibers including the glass fiber used in all our experiments, are coated with chemicals such as epoxy, resin, and silane, the layer of which is called sizing. That sizing is likely to induce its own surface anchoring for nematic SSY, considering main components of sizing are hydrophobic and typical glass surface is hydrophilic. Experimentally, the influence of sizing was observed. We placed glass fiber with sizing and one undergone plasma-cleaning in coexistence phase of SSY, and obtained images as Fig. 25 Typically, in coexistence phase, a nematic SSY droplet of hydrophilic nature in surrounding isotropic matrix has the contact angle of zero on glass surface, as in Fig. 25(b). But the sizing of hydrophobic nature increases the contact angle to about 90°, as in Fig. 25(a). This difference convinces us of the influence of sizing on nematic SSY. In fact, small amount of chemicals survives thorough plasma-cleaning in a horn shape, and it is exhibited in AFM images, Fig. 28, as white objects. However, even with those horny residual chemicals, the glass fiber was used for parallel cell experiment and took the uniaxial configuration, as reflecting little influence of the horny chemicals. As predicted, the glass fiber with sizing results in ununiform intensity in parallel cell experiment (Fig. 11). Therefore, we can conclude the plasma-cleaning process that removes fiber's chemical layer is necessary to obtain degenerate planar anchoring condition.
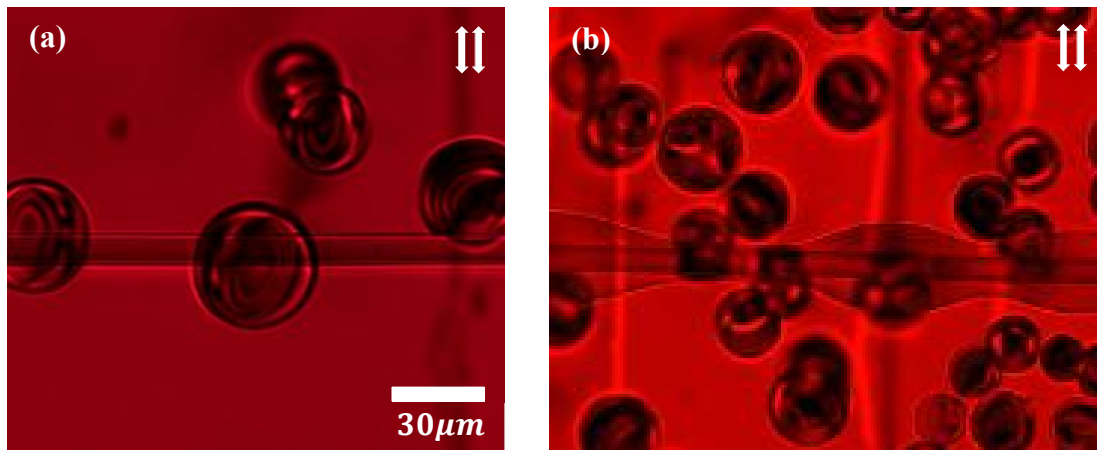

Figure 25. Wetting phenomena on glass fibers.
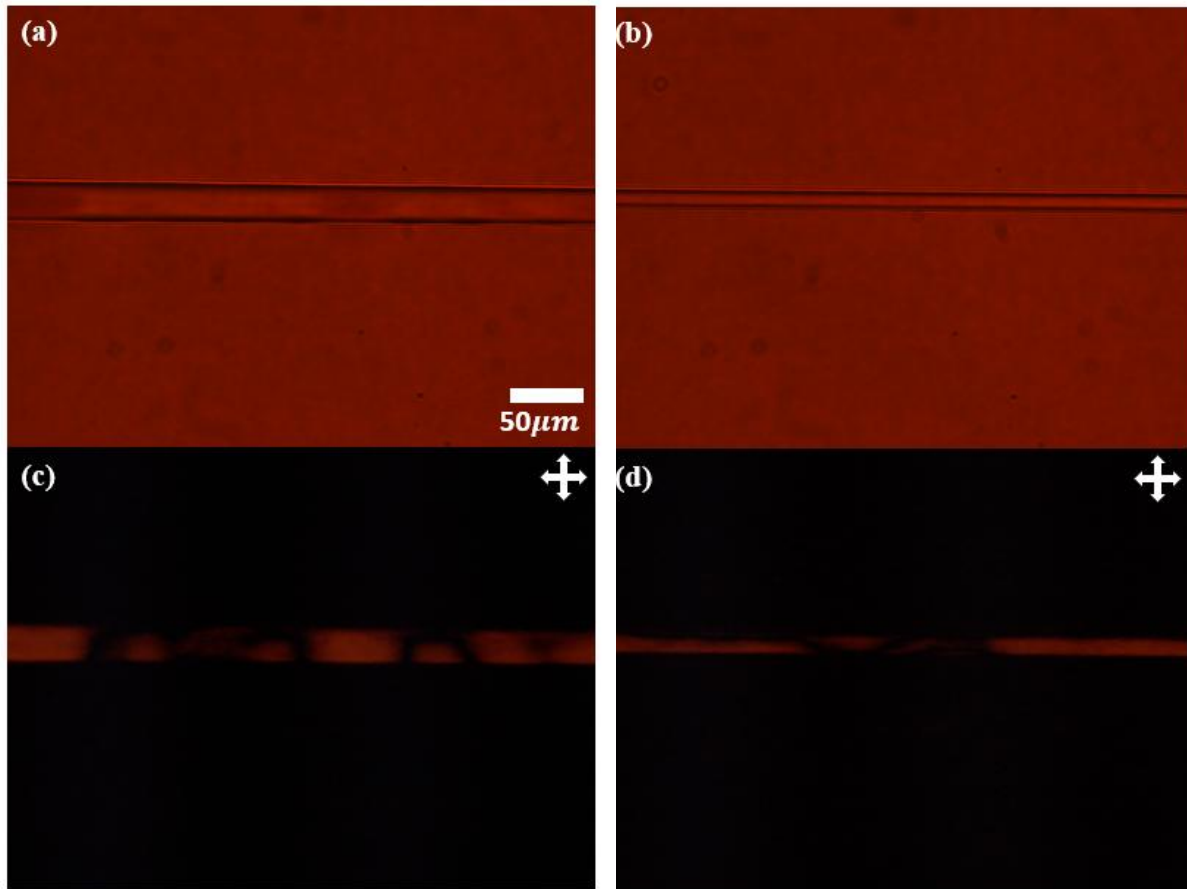(a) Glass fiber with sizing. (b) Glass fiber plasma-cleaned

Figure 26. Irregular brightness from glass fibers without degerenate planar anchoring.

To guarantee degenerate planar anchoring, glass fiber must not have any micro-scaled grooves on its surface. Given that micro-scaled grooves play a role of easy axes on glass surface, glass fiber's surface was examined by AFM to see if it has any grooved structure. The AFM images of glass fiber's surface below, reveal glass fiber has micro-groove-free surface. Of the two plasma-cleaned glass fibers, only one was polished by sandpaper, product. Both fibers' surface were examined by AFM and surface 2D view of from the top and cross-section profiles are obtained as Fig. 27. In the cross-section profile or rubbed fiber, the rubbing-scratch that typically induces surface directors' alignment is clearly probed. Whereas in the profile of unpolished fiber, no meaningful grooves are discovered. The nanometer scaled saw-teeth like fluctuations of both profiles originate from resolution limit of the AFM, not actual fluctuation of fiber's surface. That measurement inaccuracy also can be seen in a lengthwise section profile.
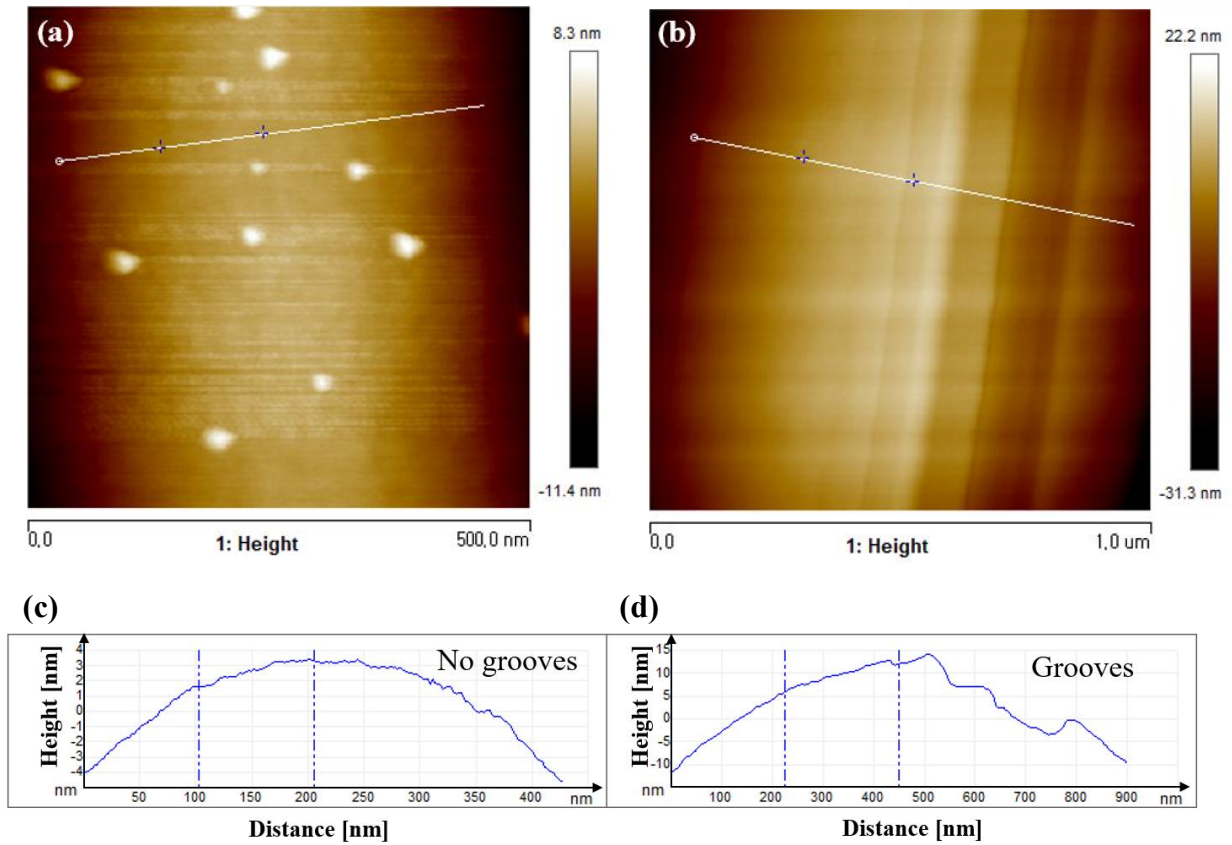
Figure 27. AFM images of gibers and cross-section profiles.

(a) glass fiber plasma-cleaned, (b) glass fiber polished, (c) cross-section profile of (a), and (d) cross-section profile of (b)
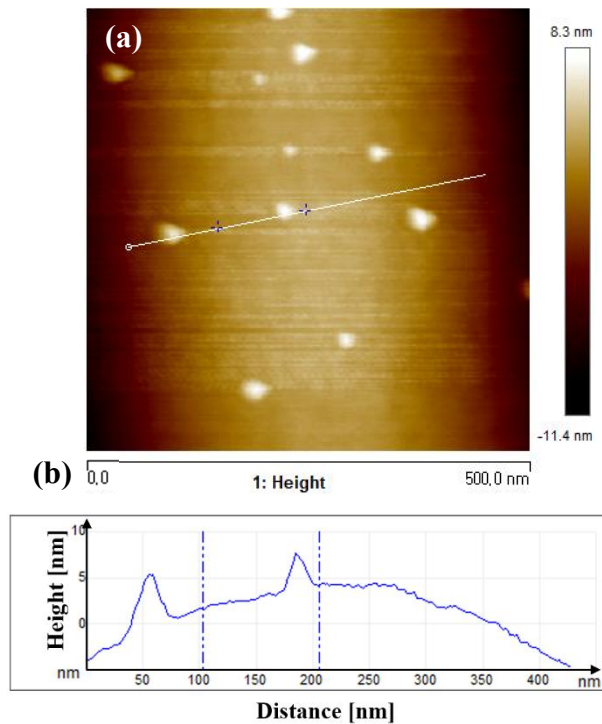

Figure 28. AFM image of plasma-cleaned glass fiber2

7 Appendix

Mathematica code for solving Laplace equation

```
ClearAll["`*"]

bandwidth = 10.0;

vvvv = Pi/2;

diameter = 13;

k = 8;

k2 = 0.8;

yprime[y_] = y/Sqrt[k/k2];

zprime[z_] = z;

uu[yprime_] =
  yprime (1 + ((Sqrt[k/k2] - 1)/(Sqrt[k/k2] + 1))^2)/(diameter/2);

vv[zprime_] =
  zprime (1 + ((Sqrt[k/k2] - 1)/(Sqrt[k/k2] + 1))^2)/(diameter/2);

yy[uu_, vv_] =
  Re[((uu + I vv) +
        Sqrt[(uu + I vv)^2 + 4 (Sqrt[k/k2] - 1)/(Sqrt[k/k2] + 1)])/2];

zz[uu_, vv_] =
  Im[((uu + I vv) +
        Sqrt[(uu + I vv)^2 + 4 (Sqrt[k/k2] - 1)/(Sqrt[k/k2] + 1)])/2];

u[yy_, zz_] = 0.5 (yy + yy/(yy^2 + zz^2));

v[yy_, zz_] = 0.5 (zz - zz/(yy^2 + zz^2));


x[u_, v_] = Re[(bandwidth/Pi) ArcCosh[(u + I v)]];

s[u_, v_] = Im[(bandwidth/Pi) ArcCosh[(u + I v)]];

phixs[x_,
    s_] = (2 vvvv/
        Pi) ArcTan[(Sin[(Pi/bandwidth) s])/(Sinh[(Pi/bandwidth) x])];

phiuv[u_, v_] = phixs[x[u, v], s[u, v]];

phiyyzz[yy_, zz_] = phiuv[u[yy, zz], v[yy, zz]];

phiuuvv[uu_, vv_] = phiyyzz[yy[uu, vv], zz[uu, vv]];

phiyprimezprime[yprime_, zprime_] = phiuuvv[uu[yprime], vv[zprime]];

phiyz[y_, z_] = phiyprimezprime[yprime[y], zprime[z]];
```

```
phi[y_, z_] = -phiyz[y, z] + Pi/2;


ContourPlot[phi[y, z], {y, 0, 30}, {z, 0, 30}, Axes -> True,
  AspectRatio -> Automatic, Contours -> 20, ContourShading -> None]


Plot3D[phi[y, z], {y, 0, 100}, {z, 0, 100}, AxesLabel -> Automatic,
  PlotRange -> {0, Pi/2}]
```

8 Reference

Ackerman, P. J., Van De Lagemaat, J., & Smalyukh, I. I. (2015). Self-assembly and electrostriction of arrays and chains of hopfion particles in chiral liquid crystals. *Nature Communications*, *6*, 1–9. https://doi.org/10.1038/ncomms7012

Čopar, S., Seč, D., Aguirre, L. E., Almeida, P. L., Dazza, M., Ravnik, M., … Žumer, S. (2016). Sensing and tuning microfiber chirality with nematic chirogyral effect. *Physical Review E*, *93*(3), 1–7. https://doi.org/10.1103/PhysRevE.93.032703

Davidson, Z. S., Huang, Y., Gross, A., Martinez, A., Still, T., Zhou, C., … Yodh, A. G. (2017). Deposition and drying dynamics of liquid crystal droplets. *Nature Communications*, *8*(May), 1–7. https://doi.org/10.1038/ncomms15642

Gwag, J. S., Lee, S. H., Han, K. Y., Kim, J. C., & Yoon, T. H. (2002). Novel cell gap measurement method for a liquid crystal cell. *Japanese Journal of Applied Physics, Part 2: Letters*, *41*(1 A/B). https://doi.org/10.1143/jjap.41.l79

Horowitz, V. R., Janowitz, L. A., Modic, A. L., Heiney, P. A., & Collings, P. J. (2005). Aggregation behavior and chromonic liquid crystal properties of an anionic monoazo dye. *Physical Review E - Statistical, Nonlinear, and Soft Matter Physics*, *72*(4), 1–10. https://doi.org/10.1103/PhysRevE.72.041710

Jeong, J., Kang, L., Davidson, Z. S., Collings, P. J., Lubensky, T. C., & Yodh, A. G. (2015). Chiral structures from achiral liquid crystals in cylindrical capillaries. *Proceedings of the National Academy of Sciences*, *112*(15), E1837–E1844. https://doi.org/10.1073/pnas.1423220112

Mcginn, C. K., Laderman, L. I., Zimmermann, N., Kitzerow, H.-S. S. H.-S., Collings, P. J., Zimmermann, N., & Kitzerow, H.-S. S. H.-S. (2013). Planar anchoring strength and pitch measurements in achiral and chiral chromonic liquid crystals using 90-degree twist cells. *Physical Review E*, *88*(6), 062513. https://doi.org/10.1103/PhysRevE.88.062513

Nayani, K., Chang, R., Fu, J., Ellis, P. W., Fernandez-Nieves, A., Park, J. O., & Srinivasarao, M. (2015). Spontaneous emergence of chirality in achiral lyotropic chromonic liquid crystals confined to cylinders. *Nature Communications*, *6*, 8067. https://doi.org/10.1038/ncomms9067

Nikkhou, M., Gleeson, H. F., & Muševič, I. (2018). Creation and topological charge switching of defect loops on a long fibre in the nematic liquid crystal. *Liquid Crystals*, 1–12. https://doi.org/10.1080/02678292.2018.1500653

Nikkhou, M., Škarabot, M., Čopar, S., Ravnik, M., Žumer, S., & Muševič, I. (2014). Light-controlled topological charge in a nematic liquid crystal. *Nature Physics*, *11*(2), 183–187. https://doi.org/10.1038/nphys3194

Nikkhou, M., Škarabot, M., & Muševič, I. (2015). Topological binding and elastic interactions of microspheres and fibres in a nematic liquid crystal. *European Physical Journal E*, *38*(3), 1–15.

https://doi.org/10.1140/epje/i2015-15023-6

Tasinkevych, M., Campbell, M. G., & Smalyukh, I. I. (2014). Splitting, linking, knotting, and solitonic escape of topological defects in nematic drops with handles. *Proceedings of the National Academy of Sciences*, *111*(46), 16268–16273. https://doi.org/10.1073/pnas.1405928111

Zhou, S., Nastishin, Y. A., Omelchenko, M. M., Tortora, L., Nazarenko, V. G., Boiko, O. P., … Lavrentovich, O. D. (2012). Elasticity of Lyotropic Chromonic Liquid Crystals Probed by Director Reorientation in a Magnetic Field. *Physical Review Letters*, *109*(3), 037801. https://doi.org/10.1103/PhysRevLett.109.037801

Acknowledgment